Supporting Information Appendix

The Future of Airborne Sulfur-Containing Particles in the Absence of Fossil Fuel Sulfur Dioxide Emissions

V. Perraud,[1] J. R. Horne,[2] A. S. Martinez,[2,3] J. Kalinowski,[4,5] S. Meinardi,[1] M. L. Dawson,[2] L. M. Wingen,[1] D. Dabdub,[2] D. R. Blake,[1] R. B. Gerber[1,4,5] and B. J. Finlayson-Pitts[1*]

[1]Department of Chemistry
University of California Irvine
Irvine, CA 92697

[2]Department of Mechanical & Aerospace Engineering
University of California Irvine
Irvine, CA 92697

[3]Now at California Air Resource Board
1001 Street
Sacramento, CA 95814

[4]Institute of Chemistry and the Fritz Haber Research Center,
the Hebrew University of Jerusalem,
Jerusalem 91904, Israel

[5]Department of Chemistry,
University of Helsinki, P.O. Box 55,
FIN-00014, Finland

October 08, 2015

1. Description of the UCI-CIT Airshed Model

The University of California, Irvine – California Institute of Technology (UCI-CIT) regional airshed model is used to simulate air quality for the three-day period August 27-29, 2005, since reliable emissions inventories and field measurements of many species are available for those dates (1). Boundary and initial conditions are based on historical values. The UCI-CIT model contains an expanded version of the Caltech atmospheric chemical mechanism (CACM) (2) and has been used in numerous other studies to simulate air quality in the SoCAB (1, 3-5). With the addition of the organosulfur compounds (OSC) oxidation mechanism (see Table S-1), the three-dimensional model contains a total of 523 reactions and 168 gas phase species, which includes chemistry that converts SO_2 to gas phase H_2SO_4 via oxidation by OH, the Criegee intermediate and the ClO radical. The barrierless reactions of the $CH_3S(O)(O)O^{\bullet}$ radical with HCHO and higher aldehydes that were determined from *ab initio* calculations were also introduced into the model assuming rate constants of 1×10^{-10} cm^3 $molecule^{-1}$ s^{-1} (see discussion below). These are the dominant reactions, but the other ones were added for completeness. In the model, the reactions with CH_4 and higher alkanes were not included because they do not appear to be as energetically favorable as the aldehydes.

The modeling domain encompasses the South Coast Air Basin (SoCAB), utilizing 994 computational cells with a 5×5 km^2 horizontal grid size. The model contains 5 vertical layers that are variable and terrain-following, spanning 0-1100 m in height. The bottom layer of the modeling domain (0-38 m), which represents ground level, is the focus of this study. The unique modeling domain includes spatially resolved emissions and contains coastal regions, urban and suburban areas, and agricultural activity around Chino. The 2005 baseline emissions inventory is documented in the 2007 Air Quality Management Plan (AQMP) formulated by the South Coast Air Quality Management District (6). However, anthropogenic SO_2 emissions have been decreasing since 2005 due to controls on the sulfur content of fossil fuels. In order to account for such decreases, ambient SO_2 concentrations in August over the period from 2004-2013 were analyzed at various locations in the SoCAB (6). As seen in Fig. S-1, peak concentrations decreased by a factor of approximately four from the 2004-2006 period to 2011-2013. Thus SO_2 emission rates (3% of which is assumed to be direct H_2SO_4 emissions) in the base model were decreased by a factor of four compared to the 2005 baseline emissions inventory to be consistent with more recent ambient data, as were the boundary and initial conditions for SO_2 and H_2SO_4.

This scenario is hereafter labeled as "representative of the years 2011-2013". Previous evaluation of the UCI-CIT model sensitivity to initial conditions suggest that two days of spin up time are required to reduce the influence of initial conditions (1). Thus, results presented here are for the third day of simulation.

The 2005 base emissions inventory includes ammonia fluxes, which are concentrated around the Chino agricultural area. In previous studies, the average ammonia concentration measured in this area between 04:00h-05:00h over six different days in 2013 was found to be 0.76 ± 0.40 ppm (1 σ) (7). Figure S-2 shows that the model-predicted NH_3 concentrations at 04:00h and 05:00h that are very similar to the measured average. This supports the accurate representation of ammonia emissions in the model. Because emission flux measurements were not possible at the time for OSC, we chose to estimate fluxes of OSC from agricultural activities in the SoCAB by simultaneously measuring OSC and NH_3 ambient concentrations adjacent to a cattle feedlot in Chino, CA (see section 2b for the details of the OSC measurements). Measurements of NH_3 were made using an cation-exchange resin cartridge as described elsewhere (7). The NH_3 concentrations were somewhat smaller in the 2014 field study (0.15 ± 0.04 ppm (1 σ)), likely due to different meteorology, but applying the ratio of the OSC concentrations to NH_3 should be a valid approach to calculating the OSC emissions for the chosen model conditions.

2. Measurements of OSC in urban and agricultural areas

2.a. Urban Emissions

There are a number of potential sources of OSC in urban areas, most of which are quantitatively ill-defined. We considered two sources here that are found in all urban areas: Human breath and pet waste. Human breath emissions were estimated as described in the text based on an average 13.8 ppb DMS in the breath of healthy human subjects (8) and a total volume of air inhaled and exhaled per day of 10,800 L (9). Emissions were distributed to each cell according to the population.

To estimate emissions from pet waste, measurements of organic sulfur compounds in the headspace of trash bins of measured mass in a residential area were performed using a high-resolution time-of-flight proton transfer reaction mass spectrometer (PTR-ToF-MS 8000, Ionicon

Analytik, hereafter cited as PTR-MS) (10, 11). The trash bins were used primarily for pet waste so emissions of OSC are attributed to that. The air sample was introduced via a heated 1/16" PEEK tubing maintained at 70°C (343 K) at a constant flow of ~145 cc min^{-1}. The instrument was operated under the standard ion drift tube conditions with a total voltage of 600 V and pressure between 2.10 and 2.16 mbar. Under these conditions, the ratio of the electric field per number density of the drift tube buffer gas molecules E/N was ~ 130 Td leading to the predominance of the cluster H_3O^+ in the ion drift tube over the higher mass water clusters (12). All sulfur compounds of interest, including methanethiol (MTO), dimethyl sulfide (DMS), dimethyl disulfide (DMDS) and dimethyl trisulfide (DMTS) have a proton affinity higher than that of water (691 kJ mol^{-1}), which results in an efficient ionization using PTR-MS (see Table S-2). Calibration of the instrument was performed using pure standards. Details are presented elsewhere (13). Mass spectra and time profiles were extracted using the PTR-MS TOF Viewer software (Ionicon Analytik version 1.4.0) using a modified Gaussian function fit for each peak individually (10). Identification of the targeted sulfur compounds was performed using accurate mass measurements and comparison with the known fragmentation of the standards (Table S-3). For accurate mass measurements, masses at *m/z* 21.0226 $(H_3{}^{18}O)^+$ and *m/z* 123.946 (common contamination peak from the Teflon gasket present in the ion source) were used as the lock masses. Methanethiol, DMS and DMDS were unambiguously identified (see Fig. S-3 and Tables S-2 and S-3); although DMTS has been previously measured from animal waste (14, 15), it was never observed in our samples.

Emissions rates of each OSC from the trash bin were measured after the PTR-MS inlet was attached to the trash bin lid and the lid placed on the top of the bin. Fluxes of individual sulfur compounds were determined by measuring their respective signals as a function of time as indicated in Fig. S-3b. Note that each bin sample was opened in between measurements to refresh the headspace. Experimentally determined emission rates for each sulfur compound were normalized by the mass of the trash bin contents. Assuming the contents are all pet waste, these measurements were then normalized to the average amount of waste per dog per year, 274 lb $year^{-1}$ (16). Emissions for each compound per dog thus obtained are as follows: 1.1×10^{17} molecules min^{-1} for CH_3SH, 1.9×10^{15} molecules min^{-1} for CH_3SCH_3 and 2.6×10^{15} molecules min^{-1} for CH_3SSCH_3. The measured emissions of the OSC as a ratio to DMS from the residential trash bins (taking DMS = 1.0) were 58:1.0:1.4 for CH_3SH: DMS: DMDS.

2.b. Canister measurements and GC-MS Analysis of Organosulfur Compounds

Air samples were collected at Chino, CA, which is located in the SoCAB, into previously evacuated 2-L electropolished stainless steel canisters between 4:23h and 5:23h local time on August 26, 2014. After collection, the canisters were analyzed in the laboratory the same day. Non-methane hydrocarbon (NMHC) analysis was performed with a gas chromatographic system equipped with multi column/detector combinations (17). The first step is a cryogenic pre-concentration in liquid nitrogen, followed by re-vaporization and injection of 1200 mL of sample at STP into a combination of three gas chromatographs (Hewlett Packard 6890), containing a total of six different column/detector combinations. The detectors used include electron capture (ECD), flame ionization (FID), and mass selective detectors (MSD). Identification of the sulfur species was performed by intercomparison of FID and MSD analysis. This feature can enhance the accuracy of the analysis by revealing the presence of co-eluting peaks. Details of the quantification of the OSC and sampling artifacts are described elsewhere (13). It should be noted that the DMDS observed in these samples can be formed by the reaction of MTO on metal surfaces (13); thus the DMDS measurements may include both DMDS and MTO.

3. Quantum Chemical Calculations

The major oxidation paths for dimethyl sulfide (DMS) (18, 19) by the hydroxyl radical (OH) are summarized in Fig. S-4. Similar pathways occur for oxidation at night by nitrate radicals (19) While many of the individual steps have been established experimentally (19), surprisingly, the gas phase mechanism of production of MSA remains unclear (20). The $CH_3S(O)(O)O^{\bullet}$ free radical is likely the key intermediate, with one possibility being its reaction with water vapor to form MSA and OH (19). However, theoretical studies show that the reverse reaction, MSA + OH, is exothermic by -10 kcal mol^{-1} (21), so that the reaction of $CH_3S(O)(O)O^{\bullet}$ radical with water must be endothermic. Quantum chemical calculations performed here confirmed that ΔH for the $CH_3S(O)(O)O^{\bullet} + H_2O$ reaction is +6 kcal mol^{-1}, consistent with the studies on the reverse reaction (21).

All geometries of isolated species were optimized using the CCSD(T) method together with Dunning's cc-pV(T+d)Z basis set (22, 23). The restricted open-shell approach as implemented in Molpro package (24) was used. Because of the system size, complexes and transition states were optimized using the MCSCF method with an active space consisting of 11 electrons distributed in 12 orbitals. At these geometries obtained using Multi-Configurational Self Consistent Field (MCSCF) method, the single point calculations using the CCSD(T)/cc-pV(T+d)Z method were performed to obtain energies for reaction profiles. Thermodynamic values were estimated using the harmonic approximation with CCSD(T)/cc-pV(T+d)Z method for all the structures, including transition states and complexes. Forces acting on atoms according to the CCSD(T) method on MCSCF optimized minima were below 10^{-3} a.u. The usage of a high level *ab initio* potential like CCSD(T) is essential in this case because of the open-shell nature of the system. A common approach for organic complexes of this and larger sizes is DFT. However, in the case of radical systems like the one studied here, DFT methods suffer from the self-interaction problem, that do not exist in post Hartree-Fock methods. In addition, studies of radical complexes require an accurate description of dynamic electron correlation effects that are offered by the CCSD(T) method. The validity of the CCSD(T) potential for similar systems was previously confirmed in the work of Jorgensen et al. (21). In our experience, the usage of MP2 method results in major differences in the structure of transition states and the height of energy barriers for studied reactions.

Another potential mechanism for the formation of MSA is hydrogen abstraction by $CH_3S(O)(O)O^{\bullet}$ radical from organic compounds, proposed earlier based on the overall thermodynamics (19, 25, 26). However, the presence of a significant energy barrier could render the reactions too slow to be of importance. This possibility was explored here using quantum chemical calculations investigating the reaction of the $CH_3S(O)(O)O^{\bullet}$ radical with methane (CH_4) or formaldehyde (HCHO). Both the total energetics of the reaction and the energy barriers can be discussed in relation to isolated reactants and products or complexes before and after the reaction. Both reactions are exoergic regardless of whether we look at isolated molecules or complexes. For the reaction with CH_4, the energy barrier from the isolated reactants is 4.6 kcal mol^{-1}, but the binding energy of 4.1 kcal mol^{-1} for the initial complex of reactants increases the effective barrier to 8.7 kcal mol^{-1}. For the reaction with HCHO, the energy barrier from the isolated reactants does not exist, as the transition state is 6.2 kcal mol^{-1} lower in energy than the

isolated reactants. However, the binding energy of 8.1 kcal mol^{-1} of the initial complex creates the energy barrier of 1.9 kcal mol^{-1} for the reaction starting from the complex. A collection of relative energies for both processes is presented in Table S-4, and the different structures for the transition states and minima species are presented in Fig. S-5. An important implication of these results is that an earlier reported enthalpy of formation (19, 27) of the $CH_3S(O)(O)O^{\bullet}$ radical (-58 kcal mol^{-1}) must be too small, with the correct value being -73 kcal mol^{-1}.

It also seems reasonable on a fundamental chemical basis that the reaction of HCHO with $CH_3S(O)(O)O^{\bullet}$ radical is faster than that of HO_2. The reaction mechanism involves first formation of collision complex between the two species. Once a collision complex of sufficient lifetime is formed, it undergoes structural changes and the reaction between the two species occurs. For two reactive species confined within a limited distance, the latter process is expected to be fast. The faster rate is thus expected for the case of more efficient complex formation. Due to the -C=O bond, formaldehyde is quite polarizable, implying a relatively strong dispersion interaction, though the molecule is small. In addition, HCHO has a substantial dipole, and interacts with $CH_3S(O)(O)O^{\bullet}$ radical both with dipole-dipole and with dipole-induced dipole effects. The hydroperoxyl radical has a smaller dipole, and is expected to be also less polarizable. Thus, HCHO is expected to have a stronger and longer range van der Waals interaction with $CH_3S(O)(O)O^{\bullet}$ radical than HO_2, and is likely to form the collision complex more efficiently. It is harder to be sure about a larger aldehyde (RCHO) versus HCHO. For sufficiently short R, the complex formation propensity of the two is probably about equal. The fact that HCHO has two available H atoms gives it an advantage for the ensuing reaction, after complex formation.

In addition, a sensitivity analysis was performed on the $CH_3S(O)(O)O^{\bullet}$ + HCHO reaction using the UCI-CIT model. Lowering the rate constant of the reaction by a factor of 10 or 100 doesn't change the domain-wide average concentration of MSA by more than 5%. This is expected since the relative contributions of reaction with HCHO vs HO_2 can be estimated from the ratio $k^{HCHO}.[HCHO]/k^{HO2}.[HO_2]$ where the rate constants are those for HCHO and HO_2 with $CH_3S(O)(O)O^{\bullet}$ radical. The domain wide average HCHO in the model is ~3 ppb compared to 0.019 ppb for HO_2, so that the two removal processes are equal for ratios of rate constants k^{HCHO}/k^{HO2} ~0.006. With $k^{HO2} = 5 \times 10^{-11}$ cm^3 $molecule^{-1}$ s^{-1}, this would correspond to $k^{HCHO} = 3 \times 10^{-13}$ cm^3 $molecule^{-1}$ s^{-1}.

4. UCI-CIT Model predictions

Figures S-6 represents the model-predicted NO_2 concentrations (ppb) at different times during the day based on the 2005 baseline emissions inventory. Figures S-7, S-8 and S-9 represent the concentrations of MSA, SO_2, and H_2SO_4, respectively, taken at different times during the day with (a) only urban emissions (left column); (b) urban and agricultural emissions (middle column) and (c) urban, agricultural, and oceanic emissions (right column). These indicate the magnitudes of the different contributions as well as differences in the spatial distributions from the three types of sources.

5. Measurements of ambient particles in Irvine, CA

Ambient submicron particle measurements were made with a high resolution time-of-flight aerosol mass spectrometer (AMS, Aerodyne) (28). Ambient aerosol is sampled through a 100 μm orifice and an aerodynamic lens, focusing particles in the range of 40-1000 nm aerodynamic diameter. Particles travel through a time of flight vacuum chamber for size measurement and are vaporized at 600 °C, the temperature used for all measurements presented here. The vapors are finally ionized by electron impact ionization and mass analyzed with a time of flight mass spectrometer.

Mass spectral analysis was performed using software packages SQUIRREL v1.56D and PIKA v1.15D, available at http://cires1.colorado.edu/jimenez-group/ToFAMSResources/ToFSoftware/index.html, with Igor Pro 6.36 (WaveMetrics, Inc., Lake Oswego, OR, USA). The default values for SQUIRREL and PIKA fragmentation tables and all ionization efficiencies were used, except for two changes. The first is a correction made in the high-resolution fragmentation table to the isotopic abundance of ^{15}NN, whose signal interferes with quantification of the CHO^+ fragment at *m/z* 29. The new value was determined by sampling through a filter to evaluate the gaseous ^{15}NN signal when the signal from particles is expected to be zero, as described in Canagaratna et al. (29). Measurements with a particle filter were carried out daily for this reason and for determination of the detection limits of NaCl and MSA. This change does not impact the identification or quantification of MSA or NaCl peaks.

The second, and more important, is the addition of the $Na^{35}Cl^+$ and $Na^{37}Cl^+$ ions to the high-resolution fragmentation table as indicators for the presence of particulate sea salt (30). Observations of $Na^{35}Cl^+$ by AMS have been reported and used to quantify particulate chloride in submicron sea salt aerosol (30, 31). Sodium chloride is not efficiently vaporized at 600° C, thus the actual mass loadings of sea salt chloride are much larger than shown in Fig. 5 in the main text. However, the presence of $NaCl^+$ ions in the mass spectra are used to show marine influence in submicron particles sampled by AMS and their possible correlation with MSA.

Figure S-10 shows an average mass spectrum for organosulfur ions from ambient particles collected in Irvine, CA. This spectrum is in good agreement with the previously reported AMS spectrum of MSA from Ge et al. (32). The major ion used for MSA identification was $CH_3SO_2^+$ (*m/z* 78.985) observed in the high-resolution mass spectrum. Additional organosulfur ions were present that are also characteristic of MSA. However, because these additional ions could also be due to other OSC, they were not used in calculating MSA mass loadings presented here. Therefore, the MSA concentrations reported are lower limits.

The observation of MSA and other OSC has been used as an indicator for marine influence in particles from coastal and non-coastal regions (32-35). However, our data show that this is not necessarily the case, even very near the coast, such as in Irvine, CA (about five miles inland from the Pacific Ocean). We show that MSA present in ambient aerosols can have continental sources, in agreement with Ge et al. (32), who observed MSA in the Central Valley of California.

6. Ambient measurements of DMS at a dairy in Central Valley (CA)

Air samples were collected into previously evacuated electropolished canisters at a dairy farm located in the Central Valley (see Fig. S-11), which is located about 28 miles south of Fresno, CA. The samples were taken during July 2010 as part of the Student Airborne Research Program (SARP) field campaign. Once in the lab, the samples were analyzed using the same technique as described above in section 2.

REFERENCES

1. Carreras-Sospedra M, Dabdub D, Rodriguez M, Brouwer J (2006) Air quality modeling in the South Coast Air Basin of California: What do the numbers really mean? . *J Air Waste Manage* 56:1184-1195
2. Griffin RJ, Dabdub D, Seinfeld JH (2002) Secondary organic aerosol. I. Atmospheric chemical mechanism for production of molecular constituents. *J Geophys Res* 107:doi:10.1029/2001JD000541
3. Nguyen K, Dabdub D (2002) NOx and VOC control and its effects on the formation of aerosols. *Aerosol Sci Tech* 36:560-572
4. Carreras-Sospedra M, Vutukuru S, Brouwer J, Dabdub D (2010) Central power generation versus distributed generation - An air quality assessment in the South Coast Air Basin of California. *Atmos Environ* 44:3215-3223
5. Chang WL, Griffin RJ, Dabdub D (2010) Partitioning phase preference for secondary organic aerosol in an urban atmosphere. *Proc Natl Acad Sci USA* 107:6705-6710
6. SCAQMD (2007) Air Quality Management Plan (AQMP) (Air Quality Management District (AQMD)) Available at http://www.aqmd.gov/home/library/clean-air-plans/air-quality-mgt-plan/2007-air-quality-management-plan
7. Dawson ML, et al. (2014) Measurement of gas-phase ammonia and amines in air by collection onto an ion exchange resin and analysis by ion chromatography. *Atm Meas Tech* 7:2733-2744
8. Van den Velde S, Nevens F, Van Hee P, Van Steenberghe D, Quirynen M (2008) GC-MS analysis of breath odor compounds in liver patients. *J Chromat B* 875:344-348
9. Phalen RF (1984) *Inhalation Studies: Foundations and Techniques* (CRC Press, Boca Raton)
10. Graus M, Muller M, Hansel A (2010) High Resolution PTR-TOF: Quantification and Formula Confirmation of VOC in Real Time. *J Am Soc Mass Spectr* 21:1037-1044
11. Jordan A, et al. (2009) A high resolution and high sensitivity proton-transfer-reaction time-of-flight mass spectrometer (PTR-TOF-MS). *Int J Mass Spectrom* 286:122-128
12. DeGouw JA, Warneke C (2007) Measurements of volatile organic compounds in the earth's atmosphere using proton-transfer-reaction mass spectrometry. *Mass Spectrom Rev* 26:223-257
13. Perraud V, Meinardi S, Blake DR, Finlayson-Pitts BJ (2015) Comparison of PTR-MS and GC-MS for determination of organosulfur compounds in air. *in preparation*
14. Meinardi S, Jin K-Y, Barletta B, Blake DR, Vaziri ND (2013) Exhaled breath and fecal volatile organic biomarkers of chronic kidney disease. *Biochim Biophys Acta* 1830:2531-2537
15. Hales K, Parker DB, Cole NA (2015) Volatile organic compound flux from manure of cattle fed diets differing in grain processing method and co-product inclusion. *Atmos Environ* 100:20-24
16. Natural Reserve Conservation Service (2005) Composting dog waste (United States Department of Agriculture WEA, suite 100, Palmer, AK 99645, www.ak.nrcs.usda.gov)

17. Colman JJ, et al. (2001) Description of the analysis of a wide range of volatile organic compounds in whole air samples collected during PEM-Tropics A and B. *Anal Chem* 73:3723-3731
18. Berndt T, Richters S (2012) Products of the reaction of OH radicals with dimethyl sulphide in the absence of NOx: Experiment and simulation. *Atmos Environ* 47:316-322
19. Barnes I, Hjorth J, Mihalopoulos N (2006) Dimethyl sulfide and dimethyl sulfoxide and their oxidation in the atmosphere. *Chem Rev* 106:940-975
20. Karl M, Gross A, Leck C, Pirjola L (2007) Intercomparison of dimethylsulfide oxidation mechanisms for the marine boundary layer: Gaseous and particulate sulfur constituents. *J Geophys Res* 112:D15304
21. Jorgensen S, Jensen C, Kjaergaard HG, Anglada JM (2013) The gas-phase reaction of methane sulfonic acid with the hydroxyl radical without and with water vapor. *Phys Chem Chem Phys* 15:5140-5150
22. Dunning TH (1989) Gaussian-basis sets for use in correlated molecular calculations. 1. The atoms boron through neon and hydrogen. *J Chem Phys* 90:1007-1023
23. Dunning TH, Peterson KA, Wilson AK (2001) Gaussian basis sets for use in correlated molecular calculations. X. The atoms aluminum through argon revisited. *J Chem Phys* 114:9244-9253
24. Werner H-J, et al. (2012) MOLPRO, version 2012, a package for ab initio programs (at http://www.molpro.net
25. Yin FD, Grosjean D, Seinfeld JH (1990) Photoxidation of dimethyl sulfide and dimethyl disulfide. I: Mechanism development. *J Atmos Chem* 11:309-364
26. Hatakeyama S, Akimoto H (1983) Reactions of OH radicals with methanethiol, dimethylsulfide and dimethyl disulfide in air. *J Phys Chem* 87:2387-23295
27. Resende SM, De Almeida WB (1999) Thermodynamical analysis of the atmospheric fate of the CH3SCH2O2 radical. *Phys Chem Chem Phys* 1:2953-2959
28. DeCarlo PF, et al. (2006) Field-deployable, high-resolution, time-of-flight aerosol mass spectrometer. *Anal Chem* 78:8281-8289
29. Canagaratna MR, et al. (2015) Elemental ratio measurements of organic compounds using aerosol mass spectrometry: characterization, improved calibration, and implications. *Atmos Chem Phys* 15:253-272
30. Nuaaman I, et al. (2015) Separating refractory and non-refractory particulate chloride and estimating chloride depletion by aerosol mass spectrometry in a marine environment. *Atmos Chem Phys Discuss* 15:2085-2118
31. Ovadnevaite J, et al. (2012) On the effect of wind speed on submicron sea salt mass concentrations and source fluxes. *J Geophys Res* 117:Artn D16201
32. Ge X, Zhang Q, Sun Y, Ruehl CR, Setyan A (2012) Effect of aqueous-phase processing on aerosol chemistry and size distributions in Fresno, California, during wintertime. *Environ Chem* 9:221-235
33. Cahill JF, Suski K, Seinfeld JH, Zaveri RA, Prather KA (2012) The mixing state of carbonaceous aerosol particles in northern and southern California measured during CARES and CalNex 2010. *Atmos Chem Phys* 12:10989-11002
34. Crippa M, et al. (2013) Identification of marine and continental aerosol sources in Paris using high resolution aerosol mass spectrometry. *J Geophys Res* 118:1950-1963

35. Gaston CJ, Pratt KA, Qin XY, Prather KA (2010) Real-time detection and mixing state of methanesulfonate in single particles at an inland urban location during a phytoplankton bloom. *Environ Sci Technol* 44:1566-1572
36. Sander SP, et al. (2011) Chemical Kinetics and Photochemical Data for Use in Atmospheric Studies. Evaluation Number 17, JPL Publication 10-6, Jet Propulson Laboratory, Pasadena, California, http://jpldataeval.jpl.nasa.gov
37. Ammann M, et al. (2015) IUPAC Task Group on Atmospheric Chemical Kinetic Data Evaluation, http://iupac.pole-ether.fr/
38. Lide DR (1994) *Handbook of Chemistry and Physics* (CRC Press, Boca Raton, FL) 74 Ed

Table S-1. Organosulfur compound oxidation mechanisms and kinetics added to model

Reaction	**Model Reaction**	**k**[a]
$CH_3SH + OH \rightarrow CH_3S + H_2O$	MTO + OH → MTA + H_2O	3.30E-11
$CH_3SCH_3 + OH \rightarrow CH_3SCH_2OO + H_2O$	DMS + OH → DMSP + H_2O	4.80E-12
$CH_3SCH_3 + OH \rightarrow CH_3S(OH)CH_3 \rightarrow CH_3SOCH_3 + HO_2$	DMS + OH → DMSO + HO_2	2.20E-12
$CH_3SCH_2OO + NO \rightarrow CH_3S + HCHO + NO_2$	DMSP + NO → MTA + HCHO + NO_2	1.20E-11
$CH_3S + O_2 \rightarrow CH_3SOO$	MTA + O_2 → MTPR	2.41E-14
$CH_3SOO \rightarrow CH_3S + O_2$	MTPR → MTA + O_2	2.30E+05
$CH_3SOO + NO \rightarrow CH_3SO + NO_2$	MTPR + NO → MTSR + NO_2	1.10E-11
$CH_3SO + O_3 \rightarrow CH_3 + SO_2 + O_2$	MTSR + O_3 → MTLR + SO_2 + O_2	4.10E-13
$CH_3SO + NO_2 \rightarrow CH_3 + SO_2 + NO$	MTSR + NO_2 → MTLR + SO_2 +NO	3.00E-12
$DMSO + OH \rightarrow CH_3S(O)OH + CH_3$	DMSO + OH → MSIA + MTLR	8.90E-11
$CH_3SSCH_3 + OH \rightarrow CH_3SH + CH_3SO$	DMDS + OH → MTO + MTSR	2.30E-10
$CH_3SSSCH_3 + OH \rightarrow CH_3SH + CH_3SSO$	DMTS + OH → MTO + MDSO	2.30E-10
$CH_3SH + NO_3 \rightarrow CH_3S + HNO_3$	MTO + NO_3 → MTA + HNO_3	9.20E-13
$CH_3SCH_3 + NO_3 \rightarrow CH_3SCH_2OO + HNO_3$	DMS + NO_3 → DMSP + HNO_3	1.10E-12
$CH_3SSCH_3 + NO_3 \rightarrow CH_3S + CH_3SO + NO_2$	DMDS + NO_3 → MTA + MTSR + NO_2	7.00E-13
$CH_3SSSCH_3 + NO_3 \rightarrow 2CH_3S + SO_2 + NO_2$	DMTS + NO_3 → 2MTA + SO_2 + NO_2	7.00E-13
$CH_3SSO + O_3 \rightarrow CH_3S + SO_2 + O_2$	MDSO + O_3 → MTA + SO_2 + O_2	4.24E-13
$CH_3SSO + NO_2 \rightarrow CH_3S + SO_2 + NO$	MDSO + NO_2 → MTA + SO_2 + NO	4.50E-12
$CH_3SOO + NO_2 \rightarrow CH_3SO + NO_3$	MTPR + NO_2 → MTSR + NO_3	2.20E-11
$CH_3S + O_3 \rightarrow CH_3SO + O_2$	MTA + O_3 → MTSR + O_2	4.90E-12
$CH_3SOO \rightarrow CH_3 + SO_2$	MTPR → MTLR + SO_2	8.00E+00
$CH_3S(O)(O) \rightarrow CH_3 + SO_2$	MSFR→ MTLR + SO_2	4.00E-01
$CH_3S(O)OH + OH \rightarrow CH_3 + SO_2 + H_2O$	MSIA + OH → MTLR + SO_2 + H_2O	9.00E-11
$CH_3SCH_2OO + HO_2 \rightarrow CH_3SCH_2OOH + O_2$	DMSP + HO_2 → HYPERA + O_2	8.80E-12
$CH_3SCH_2OO + RO_2 \rightarrow CH_3S + HCHO + RO + O_2$	DMSP + RO_2T → MTA + HCHO + RO_2T + O_2	1.00E-11
$CH_3SO + O_2 \rightarrow CH_3S(O)OO$	MTSR + O_2 → MSOX	6.26E-14
$CH_3S(O)OO \rightarrow CH_3SO + O_2$	MSOX → MTSR + O_2	5.90E+05
$CH_3S(O)OO + HO_2 \rightarrow 0.44CH_3S(O)(O) + 0.44OH$	MSOX + HO_2 → 0.44MSFR +0.44OH +	1.39E-11[b]

+ 0.41$CH_3S(O)OOH$ + 0.15MSIA + 0.15O_3	0.41HYPERB + 0.15MSIA + 0.15O_3	
$CH_3S(O)OO$ + NO → CH_3 + SO_2 + NO_2	MSOX + NO → MTLR + SO_2 + NO_2	1.00E-11
$CH_3S(O)OO$ + NO_2 → $CH_3S(O)ONO_3$	MSOX +NO_2 → SNITRA	1.20E-12
CH_3SO + NO_2 → $CH_3S(O)(O)$ + NO	MTSR + NO_2 → MSFR + NO	9.00E-12
$CH_3S(O)(O)$ + O_2 → $CH_3S(O)(O)OO$	MSFR + O_2 → MSAPER	2.10E-14
$CH_3S(O)(O)$ + O_3 → $CH_3S(O)(O)O$ + O_2	MSFR + O_3 → MSARO + O_2	3.00E-13
$CH_3S(O)(O)OO$ → $CH_3S(O)(O)$ + O_2	MSAPER → MSFR + O_2	1.95E+05
$CH_3S(O)(O)OO$ + NO → $CH_3S(O)(O)O$ + NO_2	MSAPER + NO → MSARO + NO_2	1.00E-11
$CH_3S(O)(O)OO$ + NO_2 → $CH_3S(O)(O)ONO_3$	MSAPER + NO_2 → SNITRB	1.20E-12
$CH_3S(O)(O)OO$ + HO_2 → 0.41$CH_3S(O)(O)OOH$ + 0.44$CH_3S(O)(O)O$ + 0.44OH + 0.15MSA + 0.15O_3 + 0.85O_2	MSAPER + HO_2 → 0.41HYPERC + 0.44MSARO + 0.44OH + 0.15MSA + 0.15O_3 + 0.85O_2	1.39E-11[b]
$CH_3S(O)(O)OO$ + RO_2 → 0.7$CH_3S(O)(O)O$ + 0.7RO + 0.3MSA + 0.3RCHO + O_2	MSAPER + RO_2T → 0.7MSARO + 0.7RO_2T + 0.3MSA + 0.3ALD2 + O_2	1.00E-11[b]
$CH_3S(O)(O)O$ + HO_2 → MSA + O_2	MSARO + HO_2 → MSA + O_2	5.00E-11
$CH_3S(O)(O)O$ + HCHO → MSA + HO_2 + CO	MSARO + HCHO → MSA + HO_2 + CO	1.00E-10[c]
$CH_3S(O)(O)O$ + RCHO → MSA + RO_2	MSARO + ALD2 → MSA + RO_2T	1.00E-10[c]
MTPR, MSOX, MSAPER treated as pseudo steady-state approximation (PSSA)		

[a] Units of second order rate constants are cm^3 $molecule^{-1}$ s^{-1} and units for first order reactions are s^{-1}. Rate constants taken from (36) and (37) unless otherwise indicated.

[b] From (18).

[c] Assumed to be close to diffusion controlled based on quantum chemical calculations that show the reactions are barrierless (see text).

List of Newly Added Species (not originally in Airshed):

MSA: Methanesulfonic Acid

DMS: Dimethyl Sulfide (CH_3SCH_3)

DMDS: Dimethyl Disulfide (CH_3SSCH_3)

DMTS: Dimethyl Trisulfide (CH_3SSSCH_3)

MTO: Methanethiol (Methyl Mercaptan) (CH_3SH)

DMSO: Dimethyl Sulfoxide (CH_3SOCH_3)

MTPR: Methylthiol Peroxy Radical (CH_3SOO)

MTSR: Methylsulfinyl Radical (CH_3SO)

MTLR: Methyl Radical (CH_3)

MDSO: Methyl Disulfoxide (CH_3SSO)

MTA: Methanethiolate (CH_3S)

DMSP: DMS-Derived Peroxy Radical (CH_3SCH_2OO)

MSFR: Methane Sulfonate Radical $CH_3S(O)(O)$

MSOX: $CH_3S(O)OO$

MSARO: $CH_3S(O)(O)O$

MSAPER: $CH_3S(O)(O)OO$

MSIA: $CH_3S(O)OH$

HYPERA: CH_3SCH_2OOH

HYPERB: $CH_3S(O)OOH$

HYPERC: $CH_3S(O)(O)OOH$

SNITRA: $CH_3S(O)ONO_3$

SNITRB: $CH_3S(O)(O)ONO_3$

Table S-2. Organosulfur compounds measured by PTR-MS

Compound	Formula	MW ($g\ mol^{-1}$)	Proton affinity ($kJ\ mol^{-1}$)[a]	Ions observed[c]
Methanethiol (MTO)	CH_3SH	48	773.4	49 $[M+H]^+$
Dimethyl sulfide (DMS)	CH_3SCH_3	62	830.9	63 $[M+H]^+$
Dimethyl disulfide (DMDS)	CH_3SSCH_3	94	815.3	95 $[M+H]^+$ (+ fragment at m/z 79)
Dimethyl trisulfide (DMTS)	CH_3SSSCH_3	126	b	127 $[M+H]^+$ (+ fragments at m/z 79, 81 and 93)

[a] From the Handbook of Chemistry and Physics (38).
[b] No data are available for DMTS, but this compound is expected to be similar to the other sulfur compounds.
[c] Experimental, from the analysis of pure standards.

Table S-3. Accurate mass and elemental composition of the OSC measured from trash bins.

	Accurate mass (Da)	Elemental composition	Exact mass (Da)	Absolute mass error (mDa)
MT	49.0111	$[CH_3SH + H]^+$	49.0112	-0.1
DMS	63.0266	$[CH_3SCH_3 + H]+$	63.0268	-0.2
DMDS	94.9993	$[CH_3SSCH_3 + H]^+$	94.9989	+0.4
	78.9664	CH_3SS^+	78.9676	-1.2

Table S-4. Relative energies for the reactions of $CH_3S(O)(O)O^{\bullet}$ with CH_4 or HCHO. Abbreviations for structures of complexes are the same as in the Figure S-5. ΔE_{TS} corresponds to the energy barrier for the process.

Reaction	**ΔE [kcal mol^{-1}]**	**ΔE_{TS} [kcal mol^{-1}]**
$CH_3S(O)(O)O^{\bullet} + CH_4 \rightarrow MSA + {}^{\bullet}CH_3$	-5.23	4.64
Min-1 → Min-2	-8.32	8.72
$CH_3S(O)(O)O^{\bullet} + HCHO \rightarrow MSA + {}^{\bullet}CHO$	-22.29	-6.16
Min-3 → Min-4	-22.95	1.92

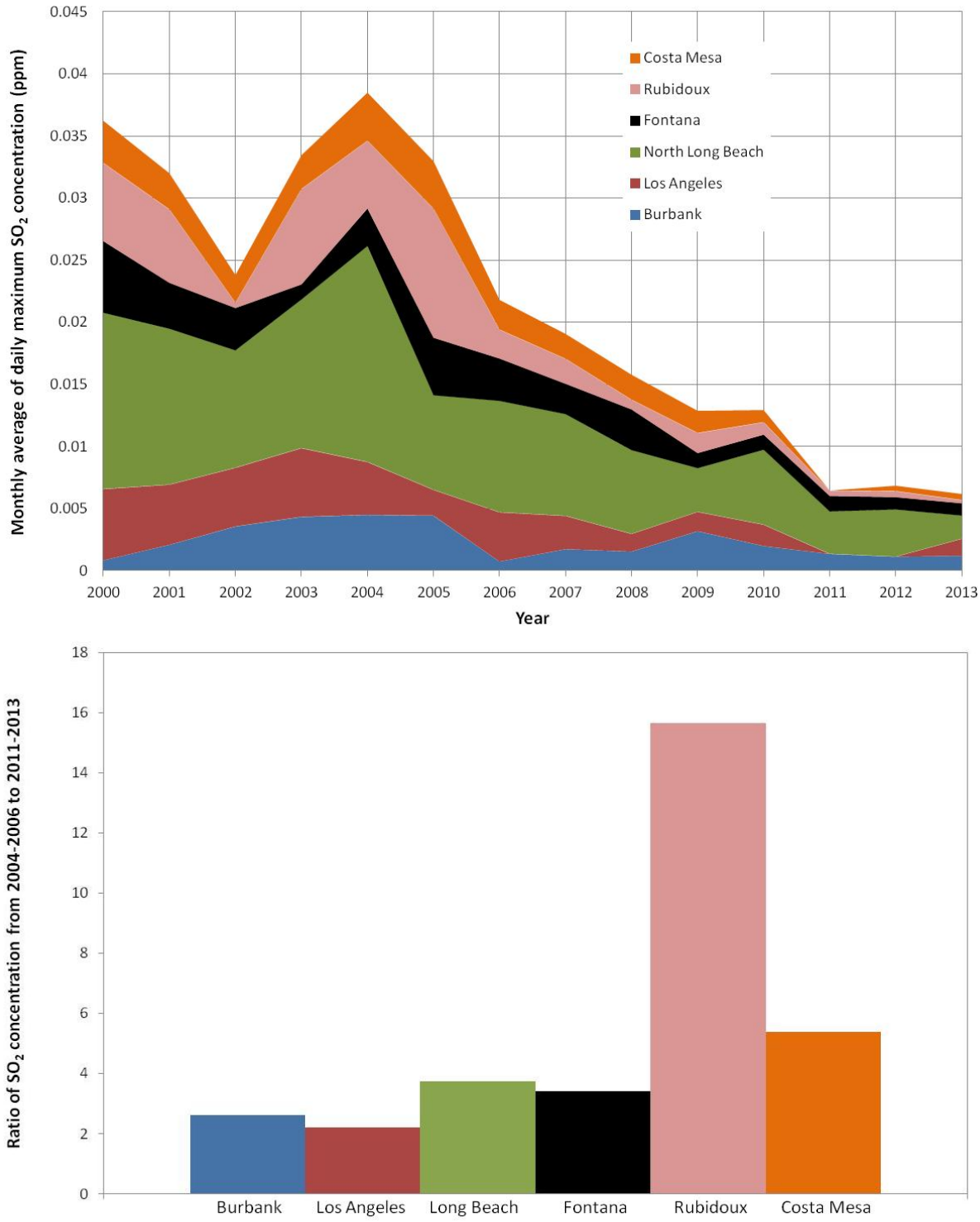

Figure S-1. (a) Evolution of the monthly average of daily maximum SO_2 concentration for the month of August for 6 sites in the South Coast Air Basin from 2000 to 2013; (b) Ratio of the average concentration of SO_2 for the month of August during 2004-2006 to that during 2011-2013. Concentration data obtained from six sites in the SoCAB. Average SO_2 concentrations are calculated by averaging the daily maximum concentrations for all days in August each year. Averages for the month of August for a 3 year period in the past (2004-2006) are compared to a

more recent 3 year period (2011, 2012 and 2013 when available) to determine the ratio of past to present SO_2 concentrations. Data source: http://www.arb.ca.gov/aqmis2/aqdselect.php

Note: Burbank – Only 13 days have reported daily average SO_2 concentration data in 2011. Some other years missing 2-5 days of data: Los Angeles – Most years missing 0-2 days of data, but 2004 missing 8 days of daily maximum SO_2 concentration data. Data for 2012 and 2013 not available; North Long Beach – Most years' data complete, a few missing 1-4 days of daily maximum SO_2 concentration data; Fontana – Most years complete or missing only a few days of daily maximum SO_2 concentration data but 2002 missing 12 days of data; Rubidoux – Data for 2013 not available but every other year complete or missing only 1-2 days of daily maximum SO_2 concentration data; Costa Mesa – Data for 2011 not available.

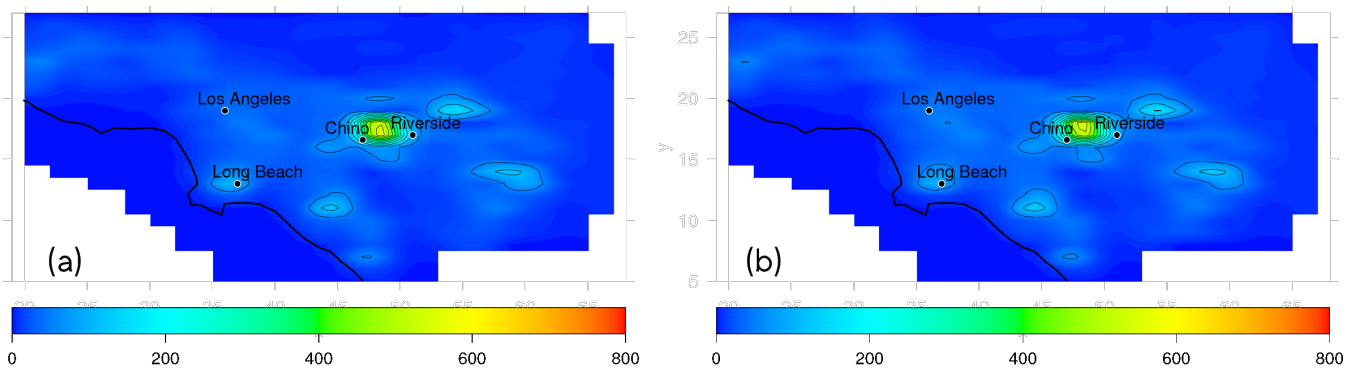

Figure S-2. Base case model-predicted NH_3 concentrations (ppb) in the SoCAB at (a) 04:00h and (b) 05:00h.

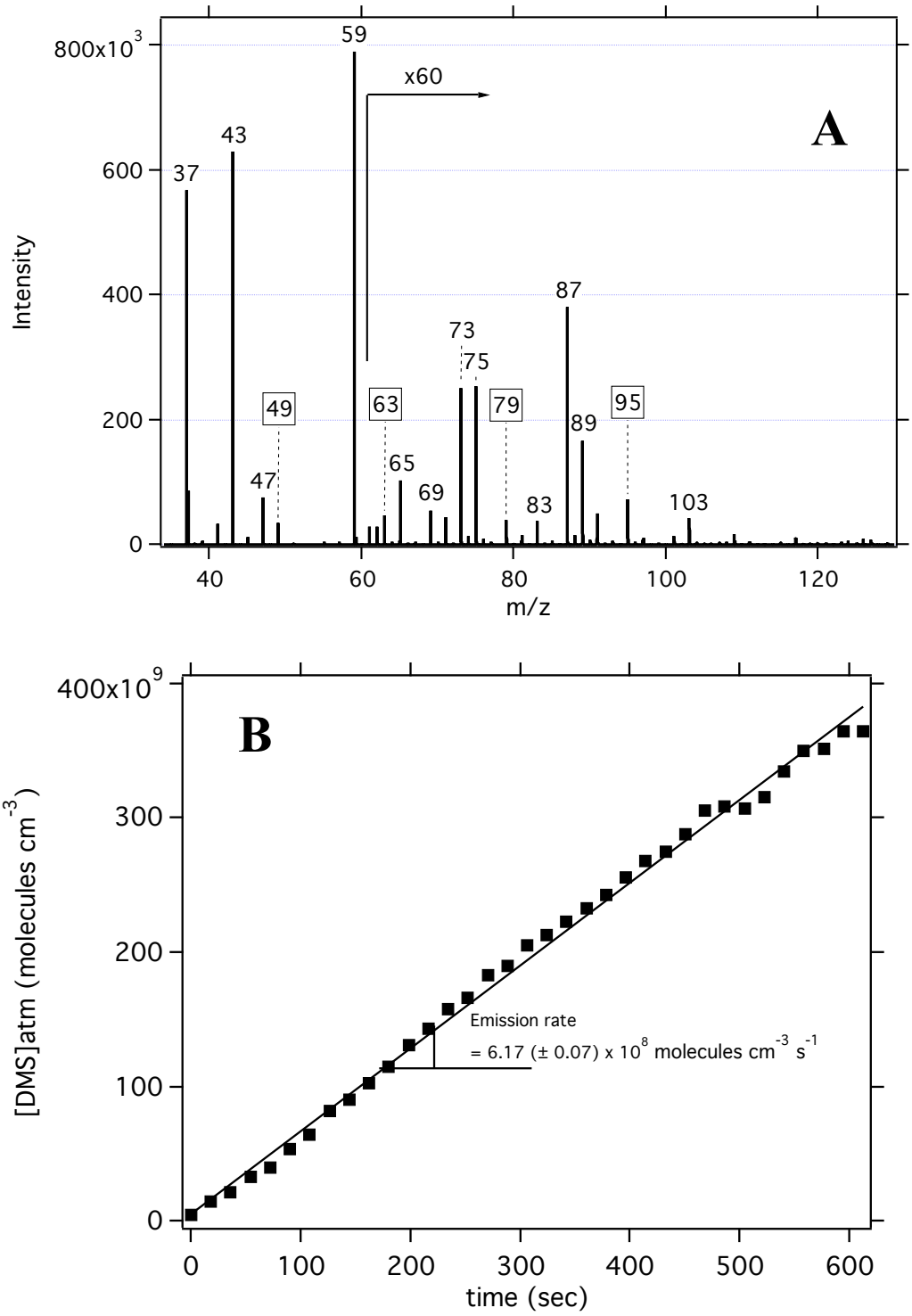

Figure S-3. (a) Typical mass spectrum from a trash bin sample (expanded by a factor of 60 above *m/z* = 62), and (b) emission curve acquired from PTR-MS measurements for the case of DMS (*m/z* 63). The peak at *m/z* 49 is assigned to MTO, at 63 to DMS and 95 and 79 to DMDS. Identification of these compounds was confirmed by the canister measurements.

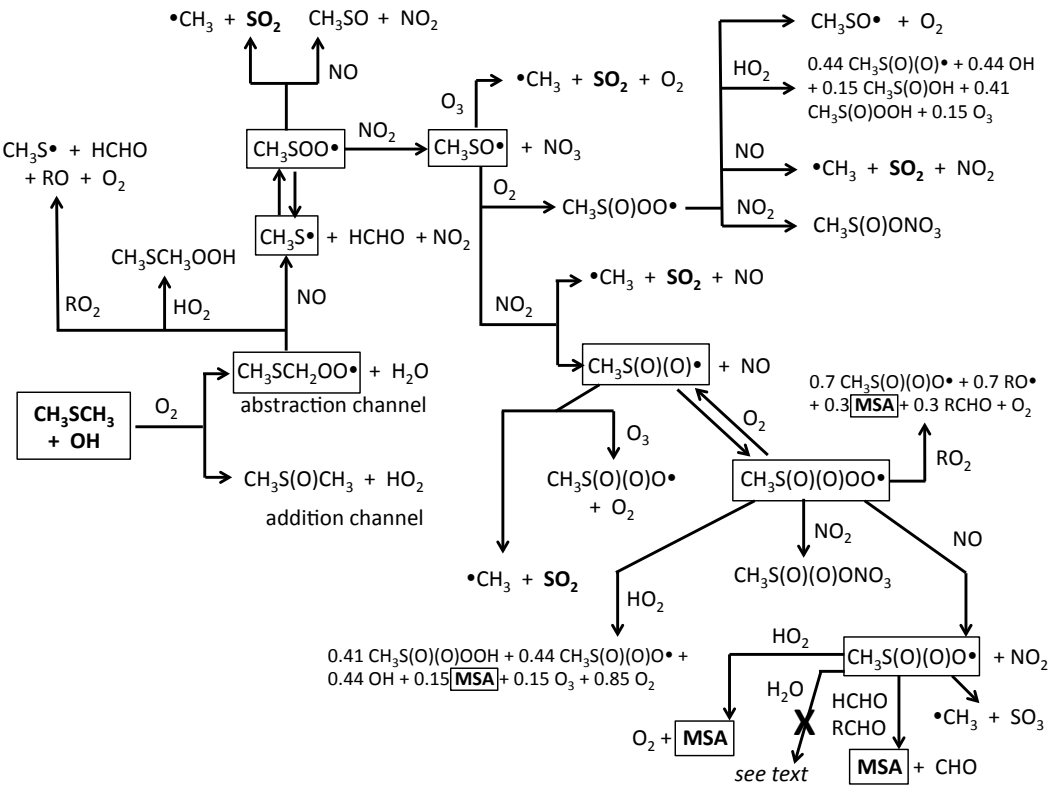

Figure S-4. Mechanism for the oxidation of dimethyl sulfide (DMS).

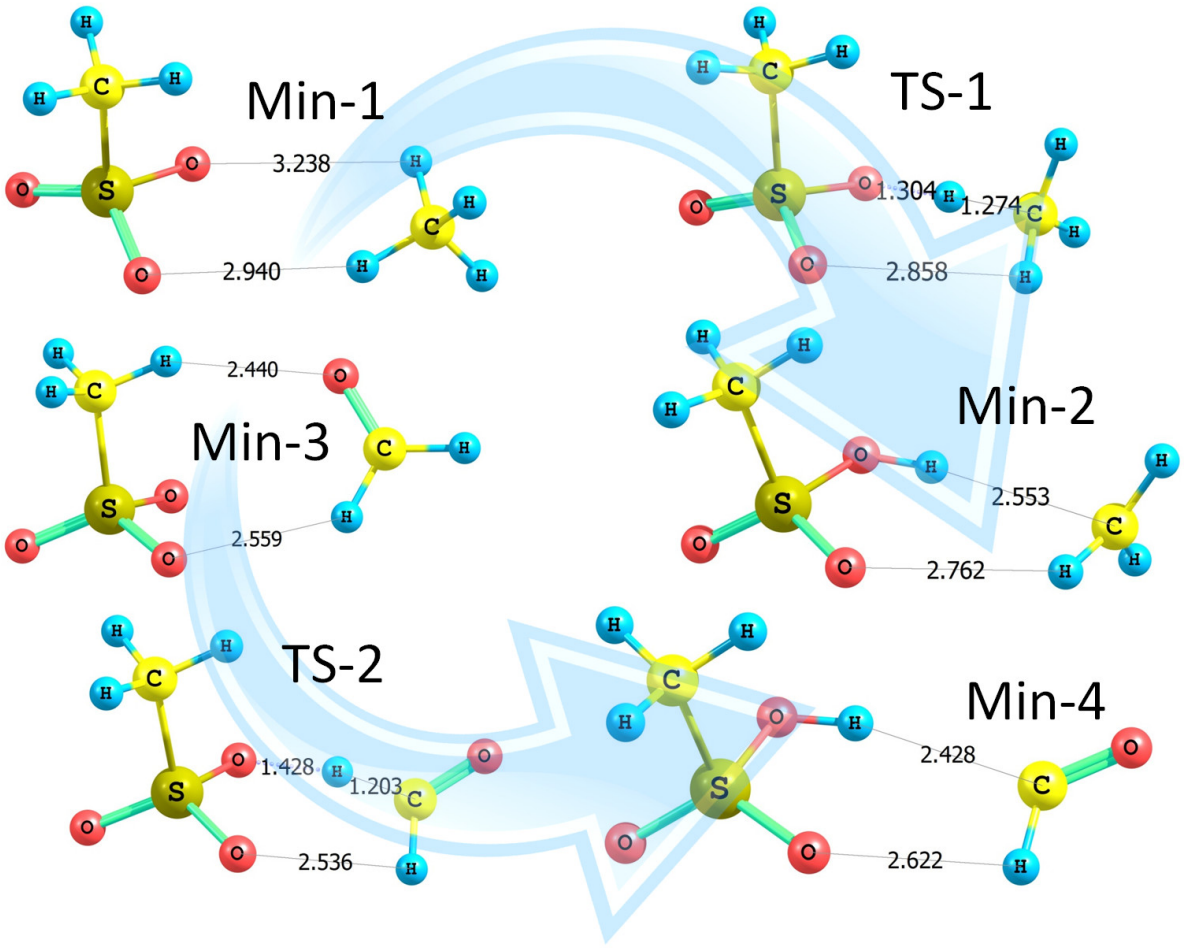

Figure S-5. Optimized geometries for complexes and transition states in the reactions of $CH_3S(O)(O)O$ with CH_4 or HCHO. Selected distances are given in Ångstroms. Geometries are optimized using MCSCF/cc-pV(T+d)Z with an active space consisting of 11 electrons in 12 orbitals.

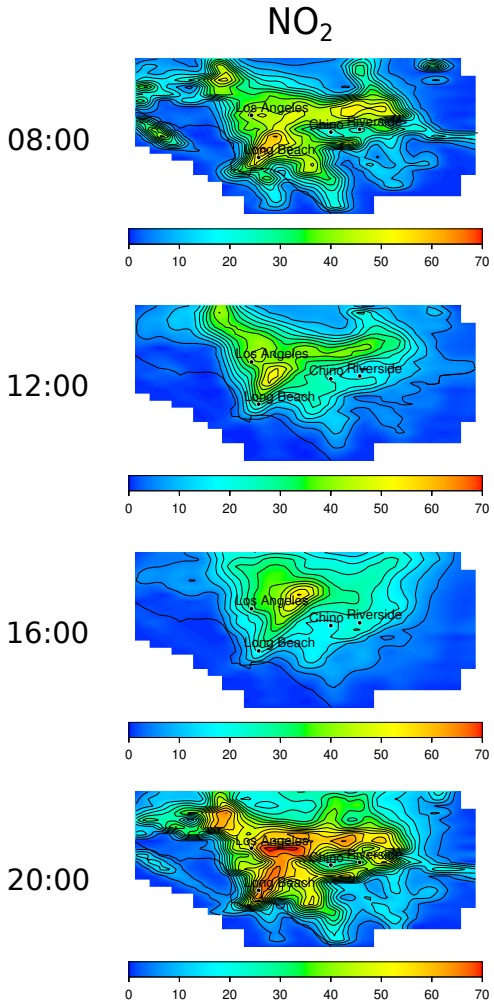

Figure S-6. Model-predicted NO_2 concentrations (ppb) at 08:00h, 12:00h, 16:00h, and 20:00h local time from the 2005 baseline emissions inventory. The concentrations, geographical and temporal distributions of NO_2 are not impacted by the SO_2/H_2SO_4 emissions scenario.

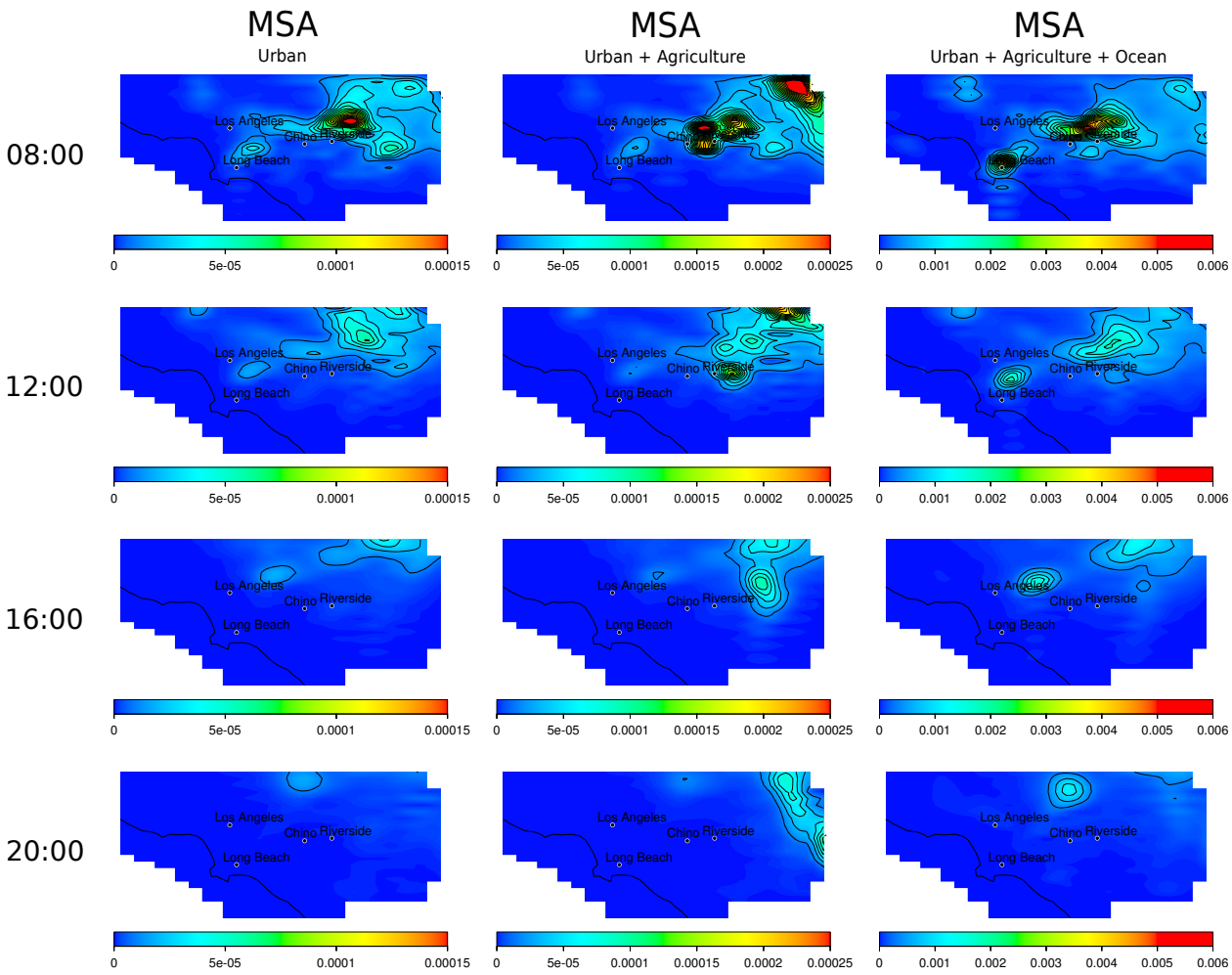

Figure S-7. Model-predicted gas phase MSA concentrations (ppb) at 08:00h, 12:00h, 16:00h, and 20:00h local time with sulfur fossil fuel emissions, boundary conditions, and initial conditions for SO_2 and H_2SO_4 set to zero. Left column: Only urban organosulfur compound emission sources (includes DMS emissions from humans and DMS, DMDS, and MTO emissions from pet waste); Middle column: Urban and agriculture organosulfur compound emission sources (left column plus DMS and DMDS emissions from Chino); Right column: Urban, agriculture, and ocean organosulfur compound emission sources (middle column plus DMS from the ocean).

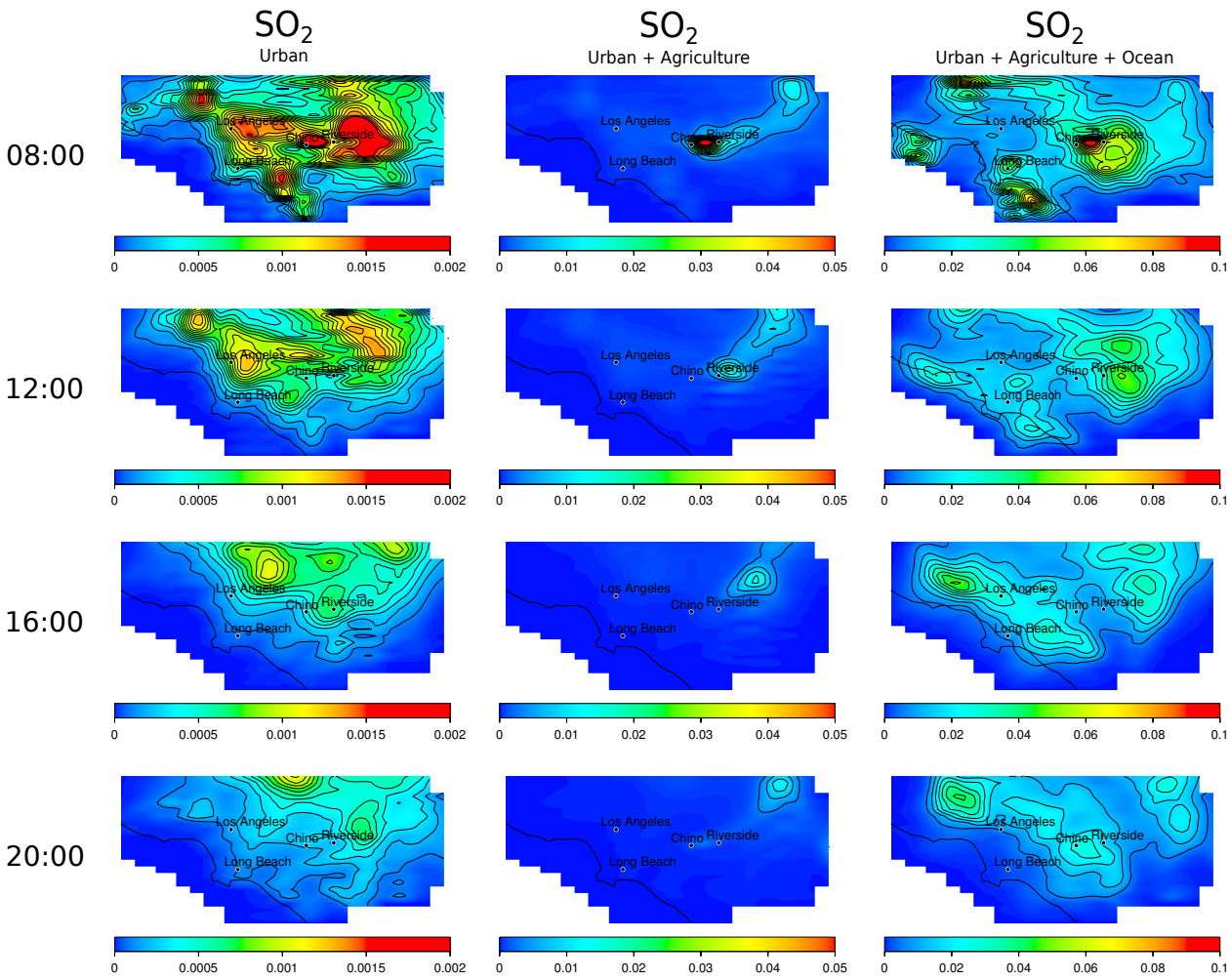

Figure S-8. Model-predicted SO_2 concentrations (ppb) at 08:00h, 12:00h, 16:00h, and 20:00h local time with sulfur fossil fuel emissions, boundary conditions, and initial conditions for SO_2 and H_2SO_4 set to zero. Left column: Only urban organosulfur compound emission sources (includes DMS emissions from humans and DMS, DMDS, and MTO emissions from pet waste); Middle column: Urban and agriculture organosulfur compound emission sources (left column plus DMS and DMDS emissions from Chino); Right column: Urban, agriculture, and ocean organosulfur compound emission sources (middle column plus DMS from the ocean).

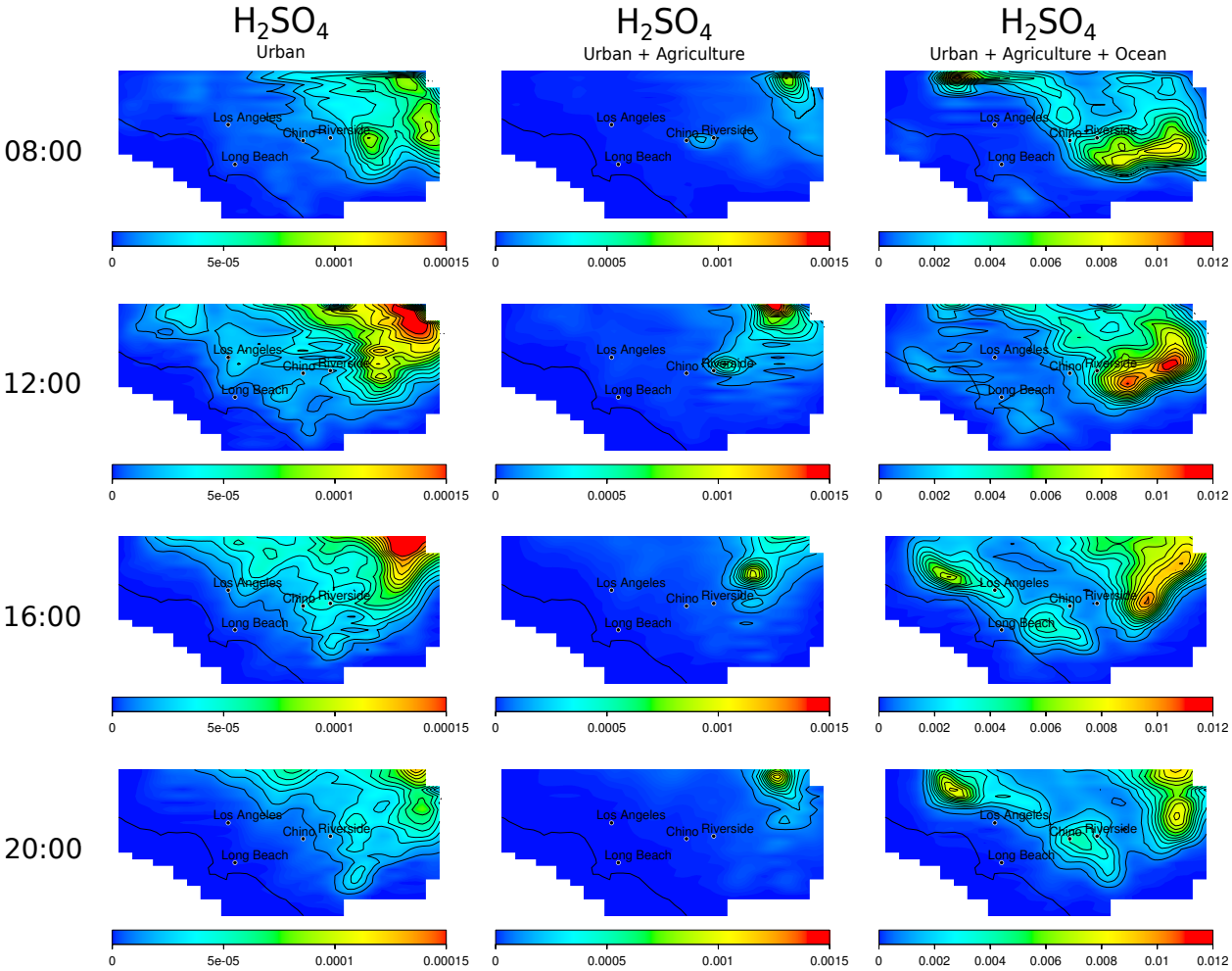

Figure S-9. Model-predicted gas phase H_2SO_4 concentrations (ppb) at 08:00h, 12:00h, 16:00h, and 20:00h local time with sulfur fossil fuel emissions, boundary conditions, and initial conditions for SO_2 and H_2SO_4 set to zero. Left column: Only urban organosulfur compound emission sources (includes DMS emissions from humans and DMS, DMDS, and MTO emissions from pet waste); Middle column: Urban and agriculture organosulfur compound emission sources (left column plus DMS and DMDS emissions from Chino); Right column: Urban, agriculture, and ocean organosulfur compound emission sources (middle column plus DMS from the ocean).

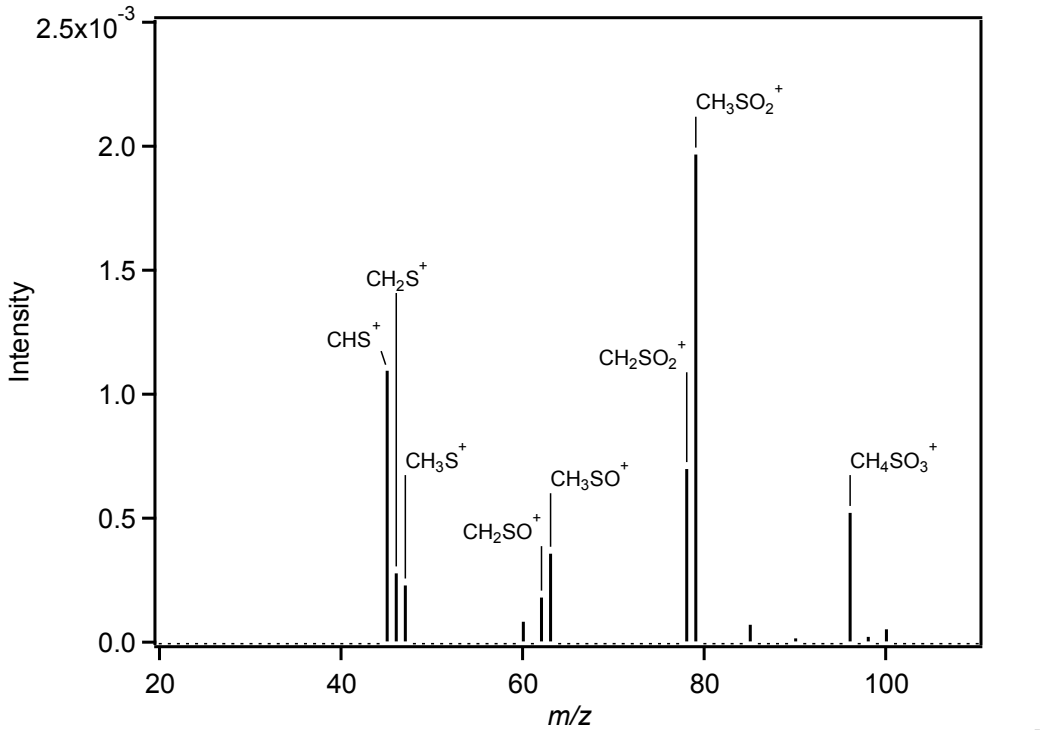

Figure S-10. Average AMS mass spectrum of organosulfur ion signals detected in ambient particles measured in Irvine, CA (data from May 14, 2012, from 10:35h to13:55h).

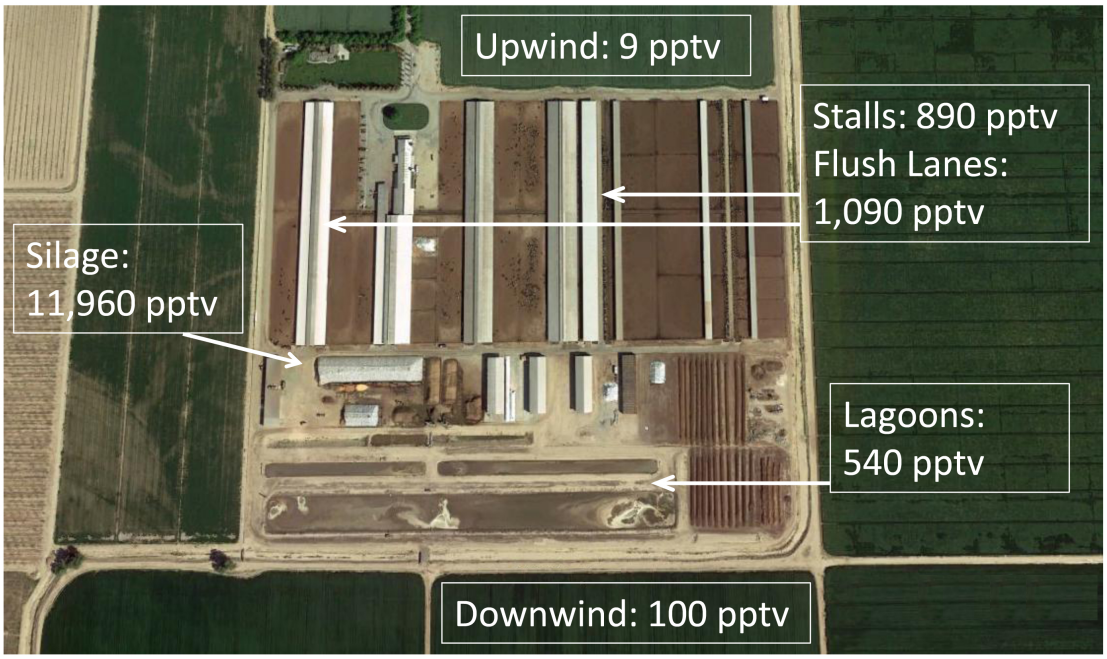

Figure S-11. Measured concentration of DMS in and around a dairy in the Central Valley of California (28 miles south of Fresno, CA). The measurements were taken from July 19 to July 20, 2010 as part of the Student Airborne Research Program (SARP) field campaign. *Imagery ©2015 DigitalGlobe, USA Farm Service Agency, Map data ©2015 Google*